HTML ABSTRACT + LINKS

Quantum yields for product formation in the 120–133 nm photodissociation of O_2

H. M. Lambert, A. A. Dixit, E. W. Davis, and P. L. Houston
Department of Chemistry and Chemical Biology, Cornell University, Ithaca, New York 14853-1301

(Received 30 July 2004; accepted 1 September 2004)

The photodissociation of O_2 in the region from 120–133 nm has been investigated using product imaging. The spectrum in this region is dominated by transitions from the ground state to the first three vibrational levels of the $E\,^3\Sigma_u^-$ state. The $O(^1D)+O(^3P)$ channel is the only product channel observed by product imaging for dissociation at either 124.4 nm or 120.4 nm. The $O(^1D_2)$ product is aligned in the molecular frame in such a way that its J vector is perpendicular to the relative velocity vector between the $O(^1D)$ and the $O(^3P)$. The variation in the anisotropy of dissociation is approximately predicted by considering transitions on individual lines and then taking into account the coherent excitation of overlapping resonances. At 132.7 nm, both the $O(^1D)+O(^3P)$ and the $O(^3P)+O(^3P)$ channels are observed with branching ratios of 0.40 ± 0.08 and 0.60 ± 0.09, respectively. At 130.2 nm, the quantum yield for production of $O(^1D)$ is 0.76 ± 0.28. © *2004 American Institute of Physics.* [DOI: 10.1063/1.1809114]

INTRODUCTION

The photochemistry of diatomic oxygen in the vacuum ultraviolet (VUV) energy range has been a subject of many investigations due to its important role in the atmospheric chemistry of the earth. Although most of the solar radiation below 170 nm is absorbed by the thermosphere, the intense Lyman-α hydrogen emission at 121.57 nm penetrates to an altitude of about 70 km.[1] In the thermosphere, the dissociation of oxygen controls the atmospheric heating rate through the deposition of kinetic energy in the photofragments. Recent interest in the heating rate stems from the connection to drag on artificial satellites, which results in premature disintegration.

O_2 absorption in the near vacuum ultraviolet is dominated by the Schumann–Runge bands, which extend between 175 nm and 205 nm and are assigned to the $B\,^3\Sigma_u^- \leftarrow X\,^3\Sigma_g^-$ electronic transition. At somewhat shorter wavelengths, between 175 and 130 nm, absorption is primarily to the Schumann–Runge continuum, which correlates predominantly to the B state asymptote of $O(^3P)+O(^1D)$, although at the higher energies there may be some contribution from a $^3\Pi_u$ state. Finally, discrete features in the spectrum are observed below 130 nm and correspond to absorption to the Rydberg states of O_2. The spectroscopy in this region is characterized by Rydberg-valence interactions. Depending on the strength of the interaction, either a diabatic or an adiabatic description of the potential energy curves is appropriate. Several *ab initio* studies have investigated the Rydberg-valence interaction in O_2.[2–8] Semiempirical estimates for the Rydberg-valence interaction have been obtained by perturbative[9–11] and coupled channel[12–20] approaches. The current study was undertaken to understand better the spectroscopy and dissociation dynamics in this Rydberg region.

In one of the earliest VUV experimental studies of O_2 absorption from its ground electronic state, Price and Collins observed diffuse bands in the far ultraviolet absorption spectrum between 65 and 130 nm.[21] Their work was followed by Tanaka's study in the 100–130 nm wavelength range that led to the identification of two new absorption bands,[22] the so-called ''second band'' and the ''third band.'' These bands are part of a progression, where the first member is the ''longest band,'' named by Price and Collins. In addition, Tanaka observed two other new progressions, later assigned as transitions from the ground state to the $3p\,\pi_u\,^1\Sigma_u^+$ and $3p\,\pi_u\,^3\Sigma_u^+$ Rydberg states.[23] Information about the Rydberg states of O_2 was also obtained by absorption studies in which the lower level was a low-lying metastable electronic state, $O_2(a\,^1\Delta)$.[23–25] Different final states were accessed by allowed transitions from the lower state due to its different symmetry from that of the ground state. Angular distributions in electron impact spectroscopy provided complementary information and helped to identify the location and symmetry of several previously unknown excited electronic states. For example, the $3s\,\sigma_g C\,^3\Pi_g$ and $3s\,\sigma_g d\,^1\Pi_g$ Rydberg states 6.5–9.5 eV, above the ground state of O_2 were first identified in electron energy loss spectra.[26,27] Several spectroscopic studies have been carried out since then in this energy regime.[28–37]

Branching ratios to dissociation products provide insight into the interactions between the Rydberg and valence states and are important to an understanding of atmospheric chemistry. The spin and energy allowed channels for dissociation at wavelengths above 110 nm are

$$O_2(X\,^3\Sigma_g^-, v=0)+h\nu$$
$$\rightarrow O(^3P)+O(^3P), \quad \lambda_{\text{threshold}}=242 \text{ nm},$$
$$\rightarrow O(^3P)+O(^1D), \quad \lambda_{\text{threshold}}=174 \text{ nm},$$
$$\rightarrow O(^3P)+O(^1S), \quad \lambda_{\text{threshold}}=133 \text{ nm}.$$

 © 2004 American Institute of Physics

Downloaded 02 Dec 2004 to 128.253.219.80. Redistribution subject to AIP license or copyright, see http://jcp.aip.org/jcp/copyright.jsp

While the reported quantum yield of the $O(^3P)+O(^1S)$ channel is small, less than 3%,[38–40] the yield for $O(^1D)$ production in the dissociation of O_2 below 174 nm is appreciable and has been measured by several authors.[41–46] Van der Zande *et al.* reported branching ratios in the predissociation of the $d\,^1\Pi_g$ and $C\,^3\Pi_g$ Rydberg states, which gave insight on the dissociation dynamics.[10] Lin *et al.* recently studied photodissociation of O_2 at 157 nm and obtained the branching ratio between $O(^3P)+O(^3P)$ and $O(^3P)+O(^1D)$ channels.[46] Lee *et al.* observed in 1977 that the yield of $O(^1D)$ varied significantly between 116 and 177 nm;[41] it was unity and nearly constant above 140 nm and oscillated between high and low values at lower wavelengths. Lacoursiere *et al.* redetermined the $O(^1D)$ quantum yields near the Lyman-α line and found them to vary from unity to 0.48 over a region of less than 0.3 nm.[43] Finally, Nee and Lee measured the photoabsorption cross section and the $O(^1D)$ quantum yield between 105–175 nm.[42,44,45] They found that the observed absorption spectrum was in good agreement with theoretical predictions of Allison *et al.*[47,48] and that the $O(^1D)$ yield in the 105–130 nm wavelength range departed significantly from unity for dissociation through the $E\,^3\Sigma_u^-$ state $v=1$ and $v=2$ levels, to 50%, for dissociation through the $E\,^3\Sigma_u^-$ state $v=0$ level at 124.4 nm.[44,45] This last result appears to contradict the finding of Lee *et al.*[41] Most of the previous work on the $O(^1D)$ quantum yield has detected this species by the fluorescence emitted following the $O(^1D)+O_2(X\,^3\Sigma^-)\rightarrow O(^3P)+O_2(b\,^1\Sigma^+)$ reaction. It has been assumed that a decrease in $O(^1D)$ yield from the $O(^1D)+O(^3P)$ channel was accompanied by an increase in the $O(^3P)+O(^3P)$ channel.

In this study, the velocity mapped product imaging technique is used to investigate photodissociation of O_2 in the longest band at 124.4 nm, in the band at 120.4 nm, at 151.7 nm, 132.7 nm, and at 130.2 nm. At each of the former two bands, the anisotropy parameter for dissociation was determined, and the quantum yield for the $O(^1D)+O(^3P)$ and $O(^3P)+O(^3P)$ channels was determined in the 124.4 nm band and at 132.7 nm and 130.2 nm. The $O(^1D_2)$ product at 124.4 nm is observed to be aligned in the molecular frame such that its angular momentum vector is perpendicular to the recoil direction, a result that may be understood based on dissociation through the $E\,^3\Sigma_u^-$ state.

EXPERIMENT

The ion imaging technique and our ion imaging time-of-flight mass spectrometer (TOFMS) have been described in more detail elsewhere.[49–51] A skimmed molecular beam of 100% O_2 was directed along the axis of a TOFMS through the center holes in the ion focusing optics. Photolysis and probe laser radiation propagated perpendicular to the molecular beam axis and intersected the beam midway between the repeller and accelerator electrodes of the ion focusing optics. The resulting neutral atomic photofragments were ionized and focused onto a position sensitive detector at the end of the TOF tube, consisting of a chevron-mounted, double microchannel plate (MCP) assembly coupled to a fast phosphor screen. Both the camera and the MCP assembly were gated in order to collect ion signal at a given mass. The ion image was recorded by a CCD camera (Xybion) and the signal was processed by IMAQ vision (National Instruments) hardware under the control of computer routines written in Labview (National Instruments).

The vacuum ultraviolet (VUV) laser radiation used for photolysis was generated by a nonlinear four wave mixing scheme in which VUV photons were produced at the difference frequency $(2\omega_1-\omega_2)$ between a two-photon resonance in krypton and a visible photon. Ultraviolet laser radiation (ω_1) at 202.25 nm $(5p'[0\ 1/2,0]\leftarrow\leftarrow 4p^6)$ or at 212.55 nm $(5p[0\,\tfrac{1}{2},0]\leftarrow\leftarrow 4p^6)$ (Ref. 52) was combined with visible laser radiation (ω_2) using dichroic mirrors and focused by a fused silica achromatic lens into a stainless steel tube containing about 5 to 20 Torr of Kr. The laser radiation and the resulting VUV radiation entered the TOFMS through a collimating lens of LiF or MgF_2 which served as the exit window of the VUV cell. VUV radiation near 124.5 nm and 130.2 nm was generated using two photons of 212.55 nm light and visible photons of 729 and 578 nm, respectively. At the lower photolysis wavelength of 120.4 nm, it was necessary to use the two-photon Kr resonance at 202.25 nm, visible photons near 630 nm and a collimating lens of LiF.

Ultraviolet laser radiation (0.5–1.0 mJ) was produced at 212.55 nm with the use of a BBO I crystal to frequency double the output of a Scanmate (Lambda Physik) dye laser pumped by the third harmonic of a GCR-270 (Spectra Physics) Nd:YAG laser. Sum frequency generated laser radiation at 202.25 nm (~0.5 mJ) was produced by first frequency doubling 606 nm dye laser light in a BBO III crystal, and then combining the fundamental and resulting 303 nm radiation in a BBO I crystal after rotating the polarization of the 303 nm light using a $\frac{1}{2}$ wave plate.

The atomic oxygen photolysis products were probed using resonance enhanced multiphoton ionization (REMPI) schemes. $O(^1D)$ was probed by (2+1) REMPI using photons at 203.7 nm which were generated in similar fashion to the 202.25 nm light described above. The laser light was focused at the intersection of the molecular beam and the photolysis radiation but in a direction counter-propagating with, and delayed by about 10 ns, with respect to the VUV light. The $O(^3P)$ atomic fragments were probed using a $(1+1')$ REMPI scheme in which the first photon excited the VUV resonance transition at 130.2 nm. Residual 202.25 nm or 212.55 nm radiation was sufficient to effect the ionization step. The generation of a second VUV wavelength in addition to the VUV photolysis wavelength was accomplished by sending a second visible laser into the VUV cell, coincident in time and spatially overlapped with the previously mentioned UV and visible lasers which generated the VUV photolysis light. This scheme was particularly advantageous since one Nd:YAG laser could be configured to pump three dye lasers simultaneously, thereby eliminating timing jitter problems. Also, the spatial overlap of the three lasers copropagating through the VUV cell and overlapping with the molecular beam was simply and reliably achieved on a daily basis.

A variety of spectra were recorded for diagnostic purposes with a photomultiplier tube used in place of the cam-

Downloaded 02 Dec 2004 to 128.253.219.80. Redistribution subject to AIP license or copyright, see http://jcp.aip.org/jcp/copyright.jsp

era. The pump–probe scheme used to produce and detect $O(^3P)$ described above by generating two different VUV wavelengths was characterized by power dependence studies. The probe visible laser was scanned over the atomic transition as a function of the laser pulse energies for each of the three lasers involved. Jet-cooled spectra of molecular oxygen also were obtained by scanning the photolysis laser while observing the O^+ signal arising from REMPI detection of the photofragments. Likewise, the spin–orbit branching ratio of $O(^3P_J)$ fragments accompanying $O(^1D)$ was determined by measuring the photomultiplier signal at each $O(^3P_J)$ resonance, correcting for the background off-resonance signal and accounting for differences in the laser energy at each resonance.

In view of the large kinetic energies released to the atomic photofragments, two different lengths of TOF tubes were used in order to ensure that fast atoms did not miss the detector. The kinetic energy release was calibrated by comparison with the ion image of $O(^3P)$ produced in the photolysis of O_2 at the $(2+1)$ REMPI detection wavelength of 225.65 nm and obtained under the same conditions of ion focusing. Wherever possible, the probe laser was scanned across the transition so that the full Doppler spread of velocities were displayed in the image. Laser energies were monitored to ensure that images were recorded under stable conditions.

Doppler scanned images of the $O(^3P_2)$ photoproduct were recorded at photolysis wavelengths of 124.4 nm and 151.75 nm in order to compare dissociation quantum yields. The latter wavelength was generated by the same four wave mixing scheme outlined above, but with the third harmonic of a Nd:YAG laser at 354.6 nm in place of the tunable visible laser (ω_2) at 729 nm. With the use of electronic shutters placed in the two (ω_2) lasers, three separate images were accumulated in sequences of 30 laser shots: one at each of the photolysis wavelengths and one with only the ionization wavelength present as background. A similar scheme was used to record $O(^3P_2)$ images at photolysis wavelengths of 130.2 and 132.7 nm. The latter wavelength was generated with the second harmonic of a Nd:YAG laser as ω_2.

All lasers were linearly polarized and arranged so that the polarization of the resulting VUV photolysis radiation was parallel to the plane of the MCP detector. In separate experiments designed to check for product angular momentum alignment, Doppler scanned images were recorded first with the polarization of the ionizing radiation parallel and then perpendicular to the detector plane.

VUV fluorescence was also detected by replacing the ion optics and TOF tube by an $f/1$ MgF_2 light collection lens and monochromator in combination with a solar blind photomultiplier tube. In these experiments, the lasers intersected an unskimmed molecular beam of O_2 10 to 30 nozzle diameters downstream of the jet orifice. The photomultiplier signal was amplified 125-fold and processed by a gated photon-counting algorithm written in Labview. Detection of the $O(^3P_2)$ dissociation product by laser induced fluorescence (LIF) at 130.2 nm provided a strong signal which was useful in optimization of the VUV generation at 124.4 nm, alignment of the light collection system, and in the calibration of the monochromator wavelength.

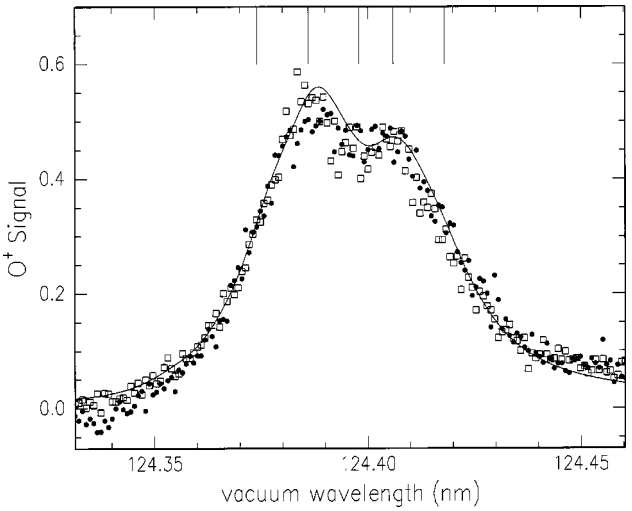

FIG. 1. Photofragment yield spectra of $O(^1D)$ (solid circles) and $O(^3P_2)$ (open squares). The solid line is a simulation at 20 K. Vertical lines on the top axis give positions where images were taken.

RESULTS

Photofragment excitation spectra

Photofragment yield spectra of $O(^1D)$ and $O(^3P_2)$ as a function of the excitation wavelength in the $O_2(E\,^3\Sigma_u^- \leftarrow X\,^3\Sigma_g^-)$ (0,0) band region around 124.4 nm are displayed in Fig. 1 along with a simulated spectrum; only the relative amplitudes have been adjusted to obtain the fit. The simulation was calculated using published spectral constants,[53,54] line strength factors for coupling behavior intermediate between Hund's cases *a* and *b*,[55] and Fano line shapes.[54] Good agreement of the simulated spectrum with the data was achieved by modeling the expansion cooling of the ground state rotational population with a Boltzmann temperature of 20 K, and by shifting the model spectrum by $+7.5$ cm^{-1}. The simulation was not convoluted with an instrument function since the VUV laser bandwidth was an order of magnitude narrower than the Fano lineshape associated with each of the rotational lines. There was no significant difference between the experimental spectra of either electronic state of the atomic oxygen photofragments. The $O(^3P_2)$ LIF excitation spectrum was very similar to those displayed in Fig. 1, although slightly broader due to a warmer expansion.

Product speed and angular distributions

Velocity-mapped images of the ionized photoproducts $O(^1D)$ and $O(^3P_2)$ were obtained at the five wavelengths denoted by the vertical lines above the spectra in Fig. 1. Some of these images are displayed in Fig. 2. In every case the images consisted of a single sharp ring with identical radii indicating that the $O(^1D)$ and $O(^3P_2)$ were coproducts of a single dissociation channel. This was confirmed by analysis of the images using inverse Abel transform algorithms which showed that the $O(^1D)$ and $O(^3P_2)$ products had the same speed. Due to magnification of the image ring

Downloaded 02 Dec 2004 to 128.253.219.80. Redistribution subject to AIP license or copyright, see http://jcp.aip.org/jcp/copyright.jsp

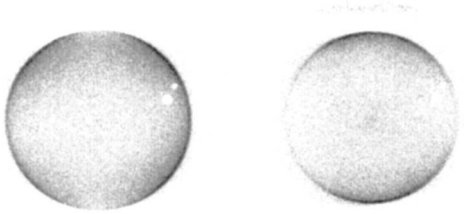

FIG. 2. Images of $O(^1D)$, left, and $O(^3P_2)$, right, following dissociation of O_2 at 124.39 nm.

by the camera and ion lenses, it was necessary to calibrate the kinetic energy released in the atomic fragments by comparison to $O(^3P_2)$ images recorded in the 225.65 nm dissociation of O_2 and analyzed in the same fashion. Figure 3 contains $O(^1D)$ and $O(^3P_2)$ product speed distributions from the photodissociation of O_2 at 124.4 nm. The speeds at which atomic products arising from other dissociation channels would be expected are also indicated.

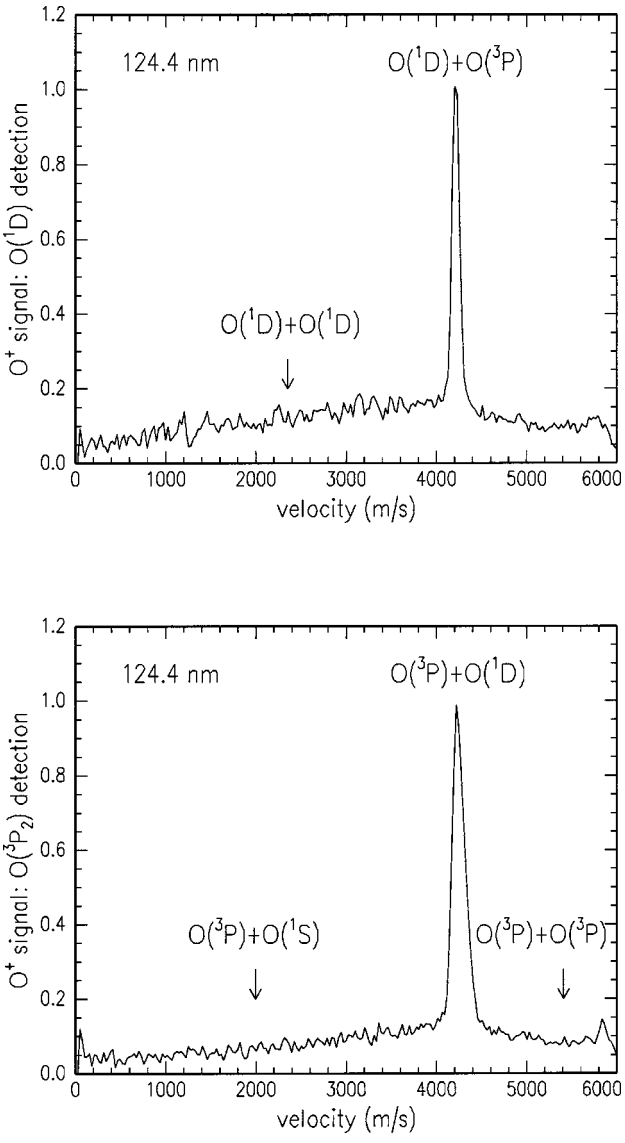

FIG. 3. Speed distributions of $O(^1D)$ (upper panel) and $O(^3P_2)$ (lower panel) produced in the 124.4 nm photodissociation of O_2.

TABLE I. Angular distributions of atomic coproducts determined from the images produced in the dissociation of O_2 near 124.4 nm.

Parameters from Eq. (1)	Dissociation products			
	$O(^1D)$	$O(^3P_2)$	$O(^3P_1)$	$O(^3P_0)$
β	-0.24 ± 0.06	0.94 ± 0.10	0.72 ± 0.12	0.56 ± 0.10
γ	-0.48 ± 0.10	-0.08 ± 0.10	0.05 ± 0.14	-0.03 ± 0.12

The apparent angular distribution of the $O(^1D)$ images depended strongly on the polarization direction of the detection laser. Use of the inverse Abel transform in the analysis presupposes axial symmetry in the image. Consequently, all of the analyzed images were recorded with polarizations of photolysis and detection lasers coparallel with the plane of the detector. Preliminary analysis involved fitting the angular distributions with a function of the form

$$I(\theta)=C\{1+\beta[P_2(\cos\theta)]+\gamma[P_4(\cos\theta)]\}, \tag{1}$$

where θ is the scattering angle with reference to the vertical axis of cylindrical symmetry (photolysis laser polarization direction), $P_2[\ ]$ and $P_4[\ ]$ are Legendre polynomials and C, β, and γ are fitting parameters. β is the usual anisotropy parameter with limiting values of $+2$ for a parallel transition and -1 for a perpendicular transition. The $P_4[\ ]$ term was included to account for alignment of the electronic angular momentum of the atomic fragments. The apparent values of β and γ for $O(^1D)$ and $O(^3P_{2,1,0})$ for the dissociation at 124.40 nm are given in Table I along with the estimates of the $\pm2\sigma$ uncertainties from the nonlinear least squares fitting program. Because the ^1D and ^3P oxygen atoms must have the same overall spatial anisotropy, the difference in angular distributions for the cofragments strongly suggests that the atomic electronic angular momentum must be aligned. This suggestion is confirmed by experiments changing the polarization of the probe laser and the related analysis, described next.

Angular distributions consistent with alignment of electronic angular momentum in cofragments of a photodissociation process were determined by fitting the following function to the data:

$$I(\theta)=C[1+\beta P_2(\cos\theta)]\Sigma_m A_m F_m(\theta). \tag{2}$$

The angular dependence of the detection step sums the contributions from the m_J levels and includes the fractional population (A_m) of each $|m_J|$ as fitting parameters. The corresponding probe frame angular detectivity functions $[F_m(\theta)]$ depend on the details of the transition probed and are well known for the two photon transitions used to detect $O(^1D)$,[56,57] so that values of β and A_m from the $O(^1D)$ data could be deduced from the images. In a similar fashion, angular distributions and fractional population of $|m_J|$ states were obtained from the $O(^3P_2)$ images, employing one photon expressions for $F_m(\theta)$.[58] Analysis of $O(^3P_0)$ images yielded angular distributions without the complication of alignment since $J=0$. A complete summary of the β and A_m values from all images is presented in Table II. The anisotropy parameters are higher in the wings of the absorption

Downloaded 02 Dec 2004 to 128.253.219.80. Redistribution subject to AIP license or copyright, see http://jcp.aip.org/jcp/copyright.jsp

TABLE II. Anisotropy parameter and $|m_J|$ populations of atomic coproducts produced in the dissociation of O_2 at 124.4 nm, 120.4 nm, and 151.75 nm. Uncertainties are $\pm 2\sigma$. Parameters are from Eq. (2).

Dissociation Wavelength (nm)	$O(^1D)$		$O(^3P_2)$		$O(^3P_0)$
	β	$A(\|m\|=1)^a/A(m=0)$	β	$A(\|m\|=1)^b/A(m=0)$	β
124.37	1.10±0.08	0.12±0.06	1.53±0.08	0	1.38±0.14
124.39	0.98±0.06	0.12±0.05	1.47±0.20	0.1	1.3 ±0.3
124.40	0.57±0.06	0.08±0.06	0.99±0.18	0.1	0.51±0.08
124.41	0.74±0.08	0.12±0.08	0.88±0.17	0.1	0.85±0.18
124.42	1.01±0.08	0.08±0.07	1.35±0.24	0.1	1.0 ± 0.2
120.40			1.1 ± 0.4	0±0.2	
151.75			2.1 ± 0.6	0±0.2	

[a] $A(|m|=2)=0$ fixed.
[b] Not sensitive to $A(|m|=2)$; $A(|m|=1)/A(m=0)$ fixed when no uncertainty is quoted.

profile with a distinct dip near the band origin. The alignment in electronic angular momentum is consistent with a predominantly $m_J=0$ distribution.

Similar images of $O(^1D)$ and $O(^3P_2)$ with single rings were recorded for excitation to the $E(^3\Sigma_u^-, v'=1)$ state at wavelengths near 120.4 nm. Again the analysis of the images demonstrated that the $O(^1D)$ and the $O(^3P)$ had the same speed and were thus coproducts of the dissociation. The calibrated $O(^1D)$ speed distribution is shown in Fig. 4 along with the expected speeds of the energetically possible dissociation channels. Parameters describing the angular distributions are also given in Table II.

Quantum yields

From the $O(^3P_2)$ image recorded in the dissociation at 132.7 nm, two rings were observed, corresponding to dissociation to $O(^1D)+O(^3P_2)$ and to $O(^3P)+O(^3P_2)$. After subtraction of the contribution from dissociation at the probe wavelength of 130.2 nm, the quantum yields for the two channels were simply determined from the integrated peak areas in the speed distribution to be 0.40±0.08 and 0.60 ±0.09, respectively. Figure 5 displays the net image after background subtraction.

Comparison of $O(^3P_2)$ signals obtained from images recorded at pairs of photodissociation wavelengths were used to determine relative quantum yields for the dissociation to $O(^1D)+O(^3P)$. Since the detection scheme was the same for each pair of dissociation wavelengths, the quantum yields Φ_i are related to the O_i signals as follows:

$$\Phi_1/\Phi_2=(O_1/O_2)(\sigma_2/\sigma_1)(SO_2/SO_1)(T_2/T_1)(I_2/I_1), \quad (3)$$

where σ is the O_2 absorption cross section, SO is the fraction of the spin–orbit population appearing as $O(^3P_2)$, T is the VUV transmission through the collimating lens, and I is the VUV laser power at the output of the Kr cell. The O atom signals were obtained by integrating over the appropriate peaks in the speed distributions. As Φ_2 is known, at 151.7 nm (Ref. 42) and at 132.7 nm (Ref. 42) (see above), then Φ_1 may be determined at 124.4 and 130.2 nm, respectively.

The VUV laser power was not measured directly but was obtained by monitoring the laser power for each of the several lasers involved in the four wave mixing scheme and using the theoretical power dependence,

$$I(\omega_{VUV})=a[I(\omega_1)]^2 I(\omega_2), \quad (4)$$

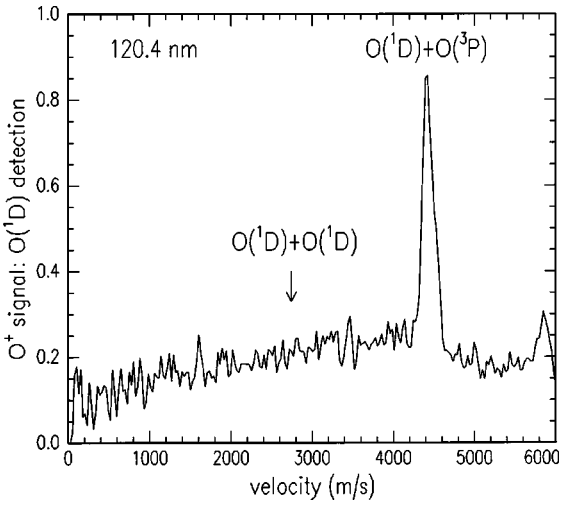

FIG. 4. Speed distribution of $O(^1D)$ produced in the 120.4 nm photodissociation of O_2.

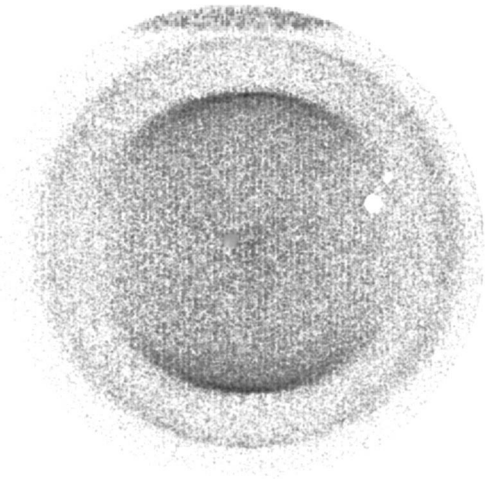

FIG. 5. Two dissociation channels are observed for O_2 excitation at 132.7 nm.

Downloaded 02 Dec 2004 to 128.253.219.80. Redistribution subject to AIP license or copyright, see http://jcp.aip.org/jcp/copyright.jsp

TABLE III. Relative $O(^1D)$ quantum yields estimated from O atom images recorded at pairs of dissociation wavelengths. Uncertainties are $\pm 2\sigma$. Parameters are from Eqs. (3) and (4).

Equation (3) Parameters	$\lambda_1 = 130.2$ nm $\lambda_2 = 132.7$ nm	$\lambda_1 = 124.4$ nm $\lambda_2 = 151.7$ nm
O_1/O_2	0.92 ± 0.30	1.28 ± 0.14
σ_2/σ_1	3.75at300K	0.086 at 20 K
$(SO)_2/(SO)_1$	~ 1	1.2 ± 0.4
T_2/T_1	1.04	1.36
I_2/I_1	0.52	0.81
Φ_1/Φ_2	1.9 ± 0.6	0.15 ± 0.04

where *a* includes various factors describing the interaction of the laser beams with the krypton.[59] Since the excitation of the two-photon Kr resonance was the same for generation of all dissociation wavelengths, the $I(\omega_1)$ term cancelled when taking the ratio I_1/I_2. The measured power dependences of the O^+ signal on each laser displayed only minor deviation from the theoretical expectations due to saturation effects. Index of refraction[60] and third order susceptibility ($\chi^{(3)}$) values[61] were used to calculate the ratio of *a* factors for different dissociation wavelengths according to Eqs. (29) and (32) in Ref. 59.

The ratios of O atom signals, absorption coefficients, spin–orbit fractions, lens transmissions, and VUV laser energies from Eqs. (3) and (4) are given in Table III along with the relative quantum yields for the pairs of dissociation wavelengths 130.2 and 132.7 nm, and 124.4 and 151.7 nm. Characterization of the angular distribution at 151.7 nm is included in Table II.

Emission from O_2 excited to the *E* state was searched for as an alternative loss process to dissociation. In the absence of the probe laser, no VUV fluorescence was detected which could be attributed to emission from excited molecular O_2 at monochromator wavelengths between 124 and 130 nm where the $E-X$ (0,0), (0,1), and (0,2) bands are expected. Franck–Condon factor calculations using Morse potentials indicate that the above three bands would comprise ~99% of the emission intensity from the *E* state $v=0$ level. Comparison of the fluorescence signal from LIF detection of the $O(^3P_2)$ dissociation product at 130.2 nm with scattered light levels in the 124–129 nm region following excitation of O_2 at 124.4 nm sets an upper limit on the ratio of quantum yields Φ_{rad}/Φ_{diss} of 10^{-6}. This observation is in agreement with the measurements of Lee *et al.*,[41] who found that photon absorption leads only to dissociation in this region.

DISCUSSION

The experimental O_2 excitation spectra taken near 124.4 nm in the $E-X$ (0,0) band for both dissociation products $O(^3P_2)$ and $O(^1D)$ agree well with each other and with the simulation based on spectral constants previously reported.[53,54] A discrepancy in the position of the origin (ν_{00}) occurs, which amounts to a difference of less than 0.01%, and which can be largely accounted for by calibration of the dye laser wavelengths. The partial resolution of the predissociation-broadened band into *P* and *R* branch envelopes reproduces the expected dominance of *R* branch line strengths for the low rotational quantum numbers populated at the experimental rotational temperature of 20 K. Modeling the predissociation widths of individual rotational lines with Fano line shapes results in good agreement with the overall shape and width of the experimental spectra. Extension of the model to include interference effects between transitions to upper levels with the same *J* but different *N* yields only minor differences in the simulated spectrum.[62]

Quantum yield determinations

The quantum yields for the two channels $O(^1D)+O(^3P)$ and $O(^3P)+O(^3P)$ following dissociation at 132.7 nm were determined to be 0.40 ± 0.08 (2σ) and 0.60 ± 0.09, respectively, assuming that these are the only two loss processes. The wavelength was well determined by the difference between the excitation of the two-photon Kr resonance at 94 092.8557 cm^{-1} and the second harmonic of the Nd:YAG laser. Previously measured $O(^1D)$ quantum yields of 0.4 (Ref. 42) and 0.37 (Ref. 41) (at 132.4 nm) are in good agreement with this determination. From the ratio of quantum yields in Table III for 130.2 and 132.7 nm dissociation, the quantum yield at 130.2 nm is thus obtained as 0.76 ± 0.28. This compares well with previously measured values of 0.82 (Ref. 42) and 0.77 (Ref. 41) (at 129.5 nm). The uncertainty in the ratio of quantum yields is mainly due to the subtraction of the noisy background from the O atom signal at the 130.2 nm dissociation. This also prevented a meaningful quantification of the yield for the $O(^3P)+O(^3P)$ channel at 130.2 nm.

The ratio of quantum yields calculated using Eqs. (3) and (4) neglects any difference in absorption cross sections between room temperature and the 20 K jet expansion conditions since this has been shown to be insignificant for the Schumann–Runge continuum.[19,63] The $O(^3P)$ spin–orbit distributions are assumed to be in the statistical limit at each dissociation wavelength since the available energies are more than 2 eV above the $O(^1D)+O(^3P)$ asymptote and 4 eV above the lower ground state channel. The *a* factor in Eq. (4) was estimated from $|\chi^{(3)}|$ values given for VUV difference frequency generation in krypton involving a different two-photon resonance than we used.[61] The difference between the two-photon energies was less than 2% of the total and should not affect the ratio of susceptibilities at the dissociation wavelengths near 130 nm. Given the success with which the ratio of quantum yields at 130.2 and 132.7 nm agree with previous measurements, it would appear that the various contributions to the *a* factor in Eq. (4), which describe the laser interactions in the nonlinear medium, were fairly well approximated.

Although excitation in the Schumann–Runge continuum at 151.7 nm and excitation to the mixed Rydberg/valence $E\,^3\Sigma_u^-$ state at 124.4 nm both result in dissociation exclusively to $O(^1D)+O(^3P)$, obtaining the ratio of quantum yields at these two wavelengths provides a more stringent test of the various approximations outlined above. While the 151.7 nm absorption cross section is insignificantly different at room temperature and at 20 K, the absorption at 124.4 nm increases by a factor of 2 between 295 and 79 K.[54] Simulation of absorption spectra of the (0,0) band near 124 nm at

Downloaded 02 Dec 2004 to 128.253.219.80. Redistribution subject to AIP license or copyright, see http://jcp.aip.org/jcp/copyright.jsp

both 79 and 20 K show that the absorption at 124.4 nm nearly doubles again at the lower temperature. The spin–orbit distributions for $O(^3P)$ accompanying $O(^1D)$ are indeed at the statistical limit at 124.4 nm, having been measured to be $(J=2):(J=1):(J=0)=(0.56\pm0.15):(0.32\pm0.13):(0.13\pm0.18)$, with uncertainties estimated to be $\pm2\sigma$. At 151.7 nm, the corresponding population ratio, $(0.66\pm0.11):(0.24\pm0.09):(0.10\pm0.07)$, appears to be slightly colder than statistical but the difference is not significantly different within the uncertainties. At the shorter wavelengths near 130 nm the population ratios are thus likely to be indistinguishable as assumed above. At longer wavelengths, two groups have measured spin–orbit population ratios in the Schumann–Runge continuum, at 157 nm.[64,65] Our results at 151.7 nm are closer to those of Matsumi and Kawasaki (0.74:0.21:0.04) than those of Huang and Gordon (0.93:0.06:0.01).

The shorter wavelength at 124.4 nm poses several problems since both the LiF collimating lens[66] and the krypton begin to absorb significantly. Absorption and transmission loss through optics is a standard problem. Modeling the VUV power generated by difference-frequency mixing near a resonance absorption in the nonlinear medium, however, is not trivial. The *a* factor of Eq. (4) includes quantities dependent on the index of refraction and the nonlinear third order susceptibility $|\chi^{(3)}|$ descriptive of the four wave mixing process. Although Bideau-Mehu *et al.* have reported a dispersion relationship with wavelength for krypton, their measurements extend down to 140 nm only.[60] The accuracy of extrapolation to shorter wavelengths on the rapidly rising part of the curve near an absorption is uncertain. Evaluation of $|\chi^{(3)}|$, involves a sum over transition matrix elements divided by energy difference terms between the energy levels considered in the numerator and the photons involved in the nonlinear mixing scheme. In difference-frequency mixing, the dominant energy difference term ideally involves only a two-photon transition with the medium transparent to all other possible single photon absorptions. This is not the case at 124.4 nm due to the Kr absorption feature at 123.6 nm. Furthermore, since the sum of the VUV and ω_2 photons is equivalent to the energy of the two-photon transition, ω_2 will also be nearly resonant with a transition between excited states. In this case where single photon absorptions become important, other processes which compete with VUV generation contribute to $|\chi^{(3)}|$. We did not attempt to calculate these additional terms or their effect on the efficiency of VUV generation. As a result, the value reported in Table III for the ratio of quantum yields $\Phi_{124.4}/\Phi_{151.7}$, based on an overestimate of the value of $|\chi^{(3)}|$ at 124.4 nm, is not very useful. Measuring the VUV laser power directly should lead to a more reliable estimate of the quantum yield at the shorter wavelength.

Nevertheless, it is clear from the absence of recoil energy peaks corresponding to the $O(^3P)+O(^3P)$ channel that, following excitation of either $O_2(E\,^3\Sigma_u^-, v=0)$ or $O_2(E\,^3\Sigma_u^-, v=1)$, the only dissociation channel produces $O(^1D)+O(^3P)$. Thus, the quantum yield of the $O(^1D)+O(^3P)$ channel must be unity at both 124.4 nm and 120.4 nm, providing that there are no other decay channels, e.g., fluorescence. From the photodissociation experiments with fluorescence detection, it was estimated by comparison with LIF signals from the $O(^3P_2)$ dissociation product, that the ratio of quantum yields for fluorescence and predissociation was less than 10^{-6}. This observation is basically in agreement with the measurements of Lee *et al.*[41] and with the 120.4 measurement of Lee and Nee,[44] but it disagrees with the value of about 0.5 inferred from Fig. 1 of Lee and Nee for excitation of $O_2(E\,^3\Sigma_u^-, v=0)$.

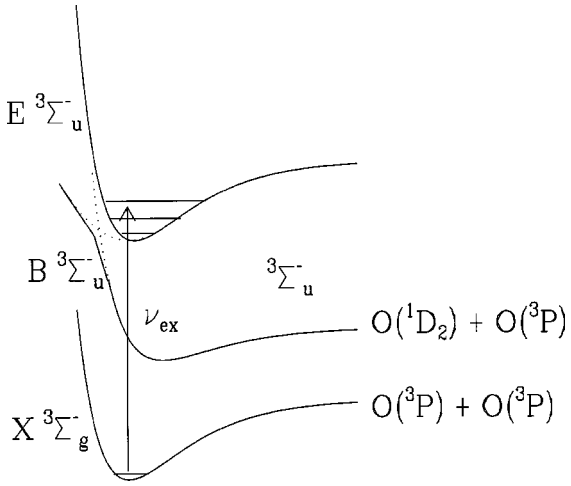

FIG. 6. Schematic diagram of O_2 *X*, *B*, and *E* states.

$O(^1D)$ product alignment

We now turn to a possible explanation for the observation that angular momentum of the $O(^1D_2)$ atomic fragment is aligned with respect to the recoil velocity in such a way that the populations of $m_J=0$ and $m_J=1$ are larger than that of $m_J=2$. Because it is clear that rotational structure is present, though not completely resolved, for absorption to $O_2(E\,^3\Sigma_u^-, v=0)$, we assume that this excited electronic state is predissociated by a state leading to the $O(^1D_2)+O(^3P)$ products. The most common predissociation is by a homogeneous mechanism,[67] for which there would be an avoided crossing between states of like symmetry; i.e., the predissociating state would also be of $^3\Sigma_u^-$ symmetry. Indeed, the work of Lewis *et al.*[12] shows that the inner wall of the *E* state is actually the diabatic continuation of the $B\,^3\Sigma_u^-$ state, as shown in Fig. 6. Thus, a simple path to products is a nonadiabatic transition between bound vibrational levels of the *E* state and the repulsive part of the *B* state.

The $B\,^3\Sigma_u^-$ state correlates, in agreement with the Wigner–Witmer rules,[53,68,69] to $O(^1D_2)+O(^3P)$, but we need to determine which of the two Σ^- states is responsible. The combination P_g+D_g gives rise to nine electronic configurations of the diatomic molecule: Σ^+, $\Sigma^-(2)$, $\Pi(3)$, $\Delta(2)$, and Φ. Each of the Σ states has zero angular momentum projection onto the internuclear axis, the Π states have ±1, the Δ states have ±2, and the Φ state has ±3, so that there are $3+3\times2+2\times2+2=15$ projection states altogether. These correspond to 15 combinations of the $(1,0,-1)$ components of the P_g atom with the $(2,1,0,-1,-2)$ components of the D_g atom. Since there are two Σ^- states among the

Downloaded 02 Dec 2004 to 128.253.219.80. Redistribution subject to AIP license or copyright, see http://jcp.aip.org/jcp/copyright.jsp

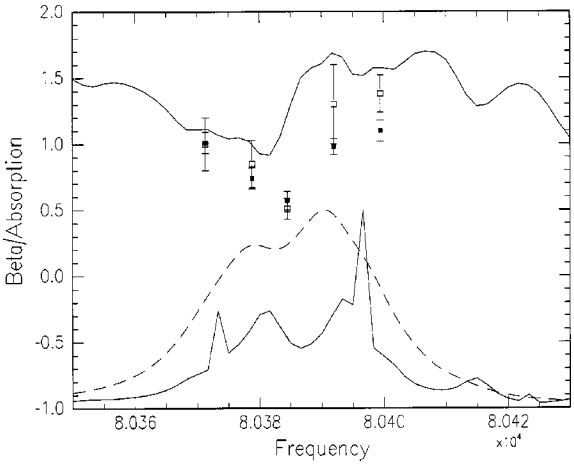

FIG. 7. Calculated variation of β with ν (upper solid curve) and absorption spectrum (lower solid curve) compared with data for β [symbols with error bars, open squares for $O(^3P_0)$ and filled ones for $O(^1D_2)$] and a curve (dashed) representing absorption (from Fig. 1).

electronic configurations, it is possible that one or both of these could cause a homogeneous predissociation of $O_2(^3\Sigma_u^-)$. According to Herzberg, one of the Σ^- states and the Σ^+ state correlate with combination of the $m_L=\pm 1$ components on the P_g atom with the $m_L=\mp 1$ components on the D_g atom, while the second Σ^- state correlates with the combination of the $m_L=0$ component on the P_g atom with the $m_L=0$ component on the D_g atom. Note that there is no $m_L=\pm 2$ component that correlates with a Σ^- state. The observation that the component of $O(^1D_2)$ angular momentum along the recoil axis is predominantly $m_L=0$, 1 is then consistent with the homogeneous predissociation of $O_2(^3\Sigma_u^-)$ by a repulsive state of Σ^- symmetry, most likely the one corresponding principally to $m_L=0$. Since the repulsive part of the $B\,^3\Sigma_u^-$ state forms the inner wall of the E state, it would seem that this is likely to be the state responsible for the predissociation. If so, dissociation along this repulsive state should also produce aligned $O(^1D_2)$. Indeed, Parker and co-workers have shown that dissociation of O_2 through the Schumann–Runge continuum region near 157 nm produced $O(^1D_2)$ atoms that are aligned with 93% in $m_L=0$.[70,71] This conclusion is also supported by our results at 151.7 nm in which the detected $O(^3P_2)$ cofragments are also found mainly in $m_L=0$. Thus, it is clear that the predissociation of the $O_2\,E\,^3\Sigma_u^-$ state is due to the repulsive region of the $B\,^3\Sigma_u^-$ state.

Variation of anisotropy parameter with wavelength

Table II gives the β parameters obtained from the angular distributions of the dissociation products $O(^1D)$, $O(^3P_2)$, and $O(^3P_0)$ at five wavelengths in the $E-X$ (0,0) band. For all three there is a pronounced dip in the value of the anisotropy parameter near the band center. The agreement of values for $O(^1D)$ and $O(^3P_0)$ is quantitative within the uncertainties. The $O(^3P_2)$ data is qualitatively similar but tend to be higher in value. Since detection of $O(^3P_2)$ involves excitation to a $^3S_1$ state, only the $m_J=0$, 1 levels are involved in the transition and the analysis is less sensitive to alignment effects.

The variation of the anisotropy parameter with wavelength across the $O_2(^3\Sigma_u^-)$ $v=0$ absorption profile is difficult to calculate because the rotational spacing and the linewidths are comparable. For isolated rotational lines, excitation produces an aligned, rotating excited state that dissociates slowly compared to a rotational period. The angular distribution can then be calculated using techniques similar to those used for NO.[51] When the rotational lines overlap, coherent excitation must be taken into account, as discussed in the Appendix. Figure 7 shows that the agreement between theory and experiment is qualitatively correct, though not quantitative.

CONCLUSION

Product imaging has been used to investigate the $O_2(E\,^3\Sigma_u^-\leftarrow X\,^3\Sigma_g^-)$ absorption in the 120–130 nm region. The products for dissociation through $v=0$, and 1 of the E state are exclusively $O(^1D)+O(^3P)$, to within the error limit of our measurement. Lee and Nee found that the quantum yield for $O(^1D)$ formation is unity for dissociation through $v=1$ and 2, but only 0.5 for dissociation through $v=0$,[44,45] while Lee *et al.*[41] found a value of unity for the wavelength corresponding to excitation of $v=0$. At other wavelengths, we found quantum yields to be in good agreement with other measurements. At 132.7 nm, both the $O(^1D)+O(^3P)$ and the $O(^3P)+O(^3P)$ channels are observed with branching ratios of 0.40 ± 0.08 and 0.60 ± 0.09, respectively. At 130.2 nm, the quantum yield for production of $O(^1D)$ is 0.76 ± 0.28.

The angular distribution of the $O(^1D_2)$ product shows that the product is aligned in the molecular frame in such a way that J is nearly perpendicular to the axis of recoil between the two oxygen atoms. This finding is consistent with a homogeneous dissociation along the repulsive wall of the B state, as might be expected from the fact that the E state is formed by an avoided crossing between the B state and a $^3\Sigma_u^-$ state leading to $O(^1D)+O(^3P)$.

The variation in the anisotropy parameter β with wavelength across the $v=0$ absorption band of the $E\leftarrow X$ transition is qualitatively in accord with a calculation similar to that used previously for NO,[51] but taking into account the coherent excitation of overlapping lines.

ACKNOWLEDGMENTS

This work was supported by the National Science Foundation under Grant No. CHE-0239903 and, in part, through the Department of Energy under Grant No. DE-FG02-88ER13934.

APPENDIX: WAVELENGTH DEPENDENCE OF β

The dependence of β on wavelength is sensitive to the electronic character of the ground and dissociating state, the rotational branch and line excited, and the lifetime of the dissociating state, which governs the linewidths of the absorption features. In the case of the $O_2\,E\,^3\Sigma_u^-$ state, the ro-

Downloaded 02 Dec 2004 to 128.253.219.80. Redistribution subject to AIP license or copyright, see http://jcp.aip.org/jcp/copyright.jsp

tational features for the $v=0$ band are incompletely resolved, so that at each dissociation wavelength a mixture of initial states is incoherently excited, and from each initial state a number of rotational transitions are coherently excited. We calculate the anisotropy parameter at each wavelength by calculating what it would be for each initial state and each transition and then by summing incoherently over the former and coherently over the latter using weights that depend on the relative populations of the initial states excited, the linewidth, and the shift from line center. This calculation is briefly described below; much of it is a one-photon version of the two-photon calculation we have presented previously for NO.[51]

The relative intensity of dissociation products at angle θ with respect to the polarization direction and for a dissociation frequency ν is given by the equation

$$I(\theta,\nu)=\sum_{\text{init levs}}\sum_{m=-J_i}^{J_i}\left[\sum_{\Omega=-1,0,1}\sum_{\text{rot trans}}S(\Omega,J_i,m,J_f)\times P(\Omega,J_i,J_f,F_i,F_f)A(J_i,J_f,F_i,F_f,\nu)d^{J_f}_{m,\Omega}(\theta)\right]^2,$$

where $S(\Omega,J_i,m,J_f)$ is the one-photon probability amplitude for the $O_2\, E\,{}^3\Sigma_u^- \leftarrow X\,{}^3\Sigma_u^-$ transition assuming Hund's case *a*,[72] $P(\Omega,J_iJ_f,F_i,F_f)$ is the correction factor for a mixture of Hund's case *a* and *b*,[55] and $A(J_i,J_f,F_i,F_f,\nu)$ is a factor that contains information on the line center and broadening for each transition as well as the population of each excited state,

$$A(J_i,J_f,F_i,F_f,\nu)=\{\exp(-T(J_i,F_i)hc/kT)F[\nu-\nu_0(J_i,J_f,F_i,F_f)]\}^{1/2},$$

where $T(J_i,F_i)$ is the term energy of the initial state, and F is a function that includes broadening parameters and gives the intensity of the absorption at ν relative to that at ν_0, the line center for the transition. We used a broadening function based on Fano line shapes,

$$F(\nu-\nu_0)=\frac{\left(q+\frac{\nu-\nu_0}{g}\right)^2}{1+\left[\frac{\nu-\nu_0}{g}\right]^2},$$

where $q=-19.2+(2.8E-05)([J_f(J_f+1)]^2$ and $g=5.6+(0.018)[J_f(J_f+1)]$, as suggested by the work of Lewis *et al.*[54] Center frequencies were calculated as $\nu_0=\nu_{00}-T_i(J_i,F_i)+T(J_f,F_f)$, where T_i and T_f give the term energies for the initial and final states, respectively, and $\nu_{00}=80\,382.8\,\text{cm}^{-1}$.

[1] J. Lilensten and M. Kretzschmar, J. Phys. IV **12**, 253 (2002).
[2] Y. Li, G. Hirsch, and R. J. Buenker, J. Chem. Phys. **108**, 8123 (1998).
[3] D. Spelsberg and W. Meyer, J. Chem. Phys. **109**, 9802 (1998).
[4] Y. Li, M. Honigmann, K. Bhanuprakash, G. Hirsch, R. J. Buenker, M. A. Dillon, and M. Kimura, J. Chem. Phys. **96**, 8314 (1992).
[5] Y. Li, M. Honigmann, G. Hirsch, and R. J. Buenker, Chem. Phys. Lett. **212**, 185 (1993).
[6] S. L. Guberman and A. Giusti-Suzor, J. Chem. Phys. **95**, 2602 (1991).
[7] S. L. Guberman, Planet. Space Sci. **36**, 47 (1987).
[8] R. J. Buenker and S. D. Peyerimhoff, Chem. Phys. Lett. **34**, 225 (1975).
[9] W. J. Van der Zande, W. Koot, and J. Los, J. Chem. Phys. **91**, 4597 (1989).
[10] W. J. Van der Zande, W. Koot, J. Los, and J. R. Peterson, J. Chem. Phys. **89**, 6758 (1988).
[11] A. Sur, L. Nguyen, and N. Nikoi, J. Chem. Phys. **96**, 6791 (1992).
[12] B. R. Lewis, S. T. Gibson, J. P. England, G. Stark, and J. B. West, J. Chem. Phys. **116**, 3286 (2002).
[13] B. R. Lewis, S. T. Gibson, S. S. Banerjee, and H. Lefebvre-Brion, J. Chem. Phys. **113**, 2214 (2000).
[14] J. S. Morrill, M. L. Ginter, B. R. Lewis, and S. T. Gibson, J. Chem. Phys. **111**, 173 (1999).
[15] J. P. England, B. R. Lewis, S. T. Gibson, and M. L. Ginter, J. Chem. Phys. **104**, 2765 (1996).
[16] B. R. Lewis, S. S. Banerjee, and S. T. Gibson, J. Chem. Phys. **102**, 6631 (1995).
[17] R. S. Friedman, M. L. Du, and A. Dalgarno, J. Chem. Phys. **93**, 2375 (1990).
[18] R. S. Friedman and A. Dalgarno, J. Chem. Phys. **93**, 2370 (1990).
[19] J. Wang, D. G. McCoy, A. J. Blake, and L. Torop, J. Quant. Spectrosc. Radiat. Transf. **38**, 19 (1987).
[20] J. Wang, A. J. Blake, D. G. McCoy, and L. Torop, J. Quant. Spectrosc. Radiat. Transf. **40**, 501 (1988).
[21] W. C. Price and G. Collins, Phys. Rev. **48**, 714 (1935).
[22] Y. Tanaka, J. Chem. Phys. **20**, 1728 (1952).
[23] M. Ogawa and K. R. Yamawaki, Can. J. Phys. **47**, 1805 (1969).
[24] F. Alberti, R. A. Ashby, and A. E. Douglas, Can. J. Phys. **46**, 337 (1968).
[25] Y. Tanaka, A. S. Jursa, F. J. Leblanc, and E. C. Y. Inn, Planet. Space Sci. **1**, 7 (1959).
[26] D. C. Cartwright, W. J. Hunt, W. Williams, S. Trajmar, and W. A. Goddard III, Phys. Rev. A **8**, 2436 (1973).
[27] T. A. York and J. Comer, J. Phys. B **16**, 3627 (1983).
[28] A. Sur, C. V. Ramana, and S. D. Colson, J. Chem. Phys. **83**, 904 (1985).
[29] A. Sur, C. V. Ramana, W. A. Chupka, and S. D. Colson, J. Chem. Phys. **84**, 69 (1986).
[30] R. O. Loo, W. J. Marinelli, P. L. Houston, S. Arepalli, J. R. Wiesenfeld, and R. W. Field, J. Chem. Phys. **91**, 5185 (1989).
[31] H. Park, L. Li, and W. A. Chupka, J. Chem. Phys. **92**, 61 (1990).
[32] H. Park, L. Li, W. A. Chupka, and H. Lefebvre-Brion, J. Chem. Phys. **92**, 5835 (1990).
[33] R. J. Yokelson, R. J. Lipert, and W. A. Chupka, J. Chem. Phys. **97**, 6153 (1992).
[34] R. J. Yokelson, R. J. Lipert, and W. A. Chupka, J. Chem. Phys. **97**, 6144 (1992).
[35] W. L. Glab, P. M. Dehmer, and J. L. Dehmer, J. Chem. Phys. **104**, 4937 (1996).
[36] B. R. Lewis, S. T. Gibson, J. S. Morrill, and M. L. Ginter, J. Chem. Phys. **111**, 186 (1999).
[37] P. O'Keeffe, T. Ridley, H. A. Sheard, K. P. Lawley, R. J. Donovan, and B. R. Lewis, J. Chem. Phys. **117**, 8705 (2002).
[38] B. A. Ridley, R. Atkinson, and K. H. Welge, J. Chem. Phys. **58**, 3878 (1973).
[39] G. M. Lawrence and M. J. McEwan, J. Geophys. Res. **78**, 8314 (1973).
[40] N. K. Bibinov, I. P. Vinogradov, and A. M. Pravilov, Opt. Spectrosc. **53**, 496 (1982).
[41] L. C. Lee, T. G. Slanger, G. Black, and R. L. Sharpless, J. Chem. Phys. **67**, 5602 (1977).
[42] J. B. Nee and P. C. Lee, J. Phys. Chem. A **101**, 6653 (1997).
[43] J. Lacoursiere, S. A. Meyer, G. W. Faris, T. G. Slanger, B. R. Lewis, and S. T. Gibson, J. Chem. Phys. **110**, 1949 (1999).
[44] P. C. Lee and J. B. Nee, J. Chem. Phys. **112**, 1763 (2000).
[45] P. C. Lee and J. B. Nee, J. Chem. Phys. **114**, 792 (2001).
[46] J. J. Lin, D. W. Hwang, Y. T. Lee, and X. Yang, J. Chem. Phys. **109**, 1758 (1998).
[47] A. C. Allison, S. L. Guberman, and A. Dalgarno, J. Geophys. Res., [Space Phys.] **87**, 923 (1982).
[48] A. C. Allison, S. L. Guberman, and A. Dalgarno, J. Geophys. Res., [Space Phys.] **91**, 10193 (1986).
[49] R. J. Wilson, J. A. Mueller, and P. L. Houston, J. Phys. Chem. A **101**, 7593 (1997).
[50] B.-Y. Chang, R. C. Hoetzlein, J. A. Mueller, J. D. Geiser, and P. L. Houston, Rev. Sci. Instrum. **69**, 1665 (1998).
[51] B. R. Cosofret, H. M. Lambert, and P. L. Houston, J. Chem. Phys. **117**, 8787 (2002).
[52] J. W. Hepburn, "Generation of coherent vacuum ultraviolet radiation: Applications to high-resolution photoionization and photoelectron spectroscopy," in *Laser Techniques in Chemistry*, edited by A. B. Myers and T. R.

Downloaded 02 Dec 2004 to 128.253.219.80. Redistribution subject to AIP license or copyright, see http://jcp.aip.org/jcp/copyright.jsp

Rizzo, Techniques in Chemistry Series, Vol. XXIII (Wiley, New York, 1995).
[53] G. Herzberg, *Spectra of Diatomic Molecules* (Van Nostrand Reinhold, New York, 1950).
[54] B. R. Lewis, S. T. Gibson, M. Emami, and J. H. Carver, J. Quant. Spectrosc. Radiat. Transf. **40**, 1 (1988).
[55] J. B. Tatum and J. K. G. Watson, Can. J. Phys. **49**, 2693 (1971).
[56] Y. Mo and T. Suzuki, J. Chem. Phys. **108**, 6780 (1998).
[57] S. M. Dylewski, J. D. Geiser, and P. L. Houston, J. Chem. Phys. **115**, 7460 (2001).
[58] R. N. Zare, *Angular Momentum* (Wiley-Interscience, New York, 1988), Chap. 5.
[59] G. Bjorklund, IEEE J. Quantum Electron. **QE-11**, 287 (1975).
[60] A. Bideau-Mehu, Y. Guern, R. Abjean, and A. Johannin-Gilles, J. Quant. Spectrosc. Radiat. Transf. **25**, 395 (1981).
[61] G. Hilber, A. Lago, and R. Wallenstein, J. Opt. Soc. Am. B **4**, 1753 (1987).
[62] F. H. Mies, Phys. Rev. **175**, 164 (1968).
[63] S. T. Gibson, H. P. F. Gies, A. J. Blake, D. G. McCoy, and P. G. Rogers, J. Quant. Spectrosc. Radiat. Transf. **30**, 385 (1983).
[64] Y. Matsumi and M. Kawasaki, J. Chem. Phys. **93**, 2481 (1990).
[65] Y. L. Huang and R. J. Gordon, J. Chem. Phys. **94**, 2640 (1991).
[66] E. G. Schneider, Phys. Rev. **49**, 341 (1935).
[67] H. Lefebvre-Brion and R. W. Field, *Perturbations in the Spectra of Diatomic Molecules* (Academic, Orlando, FL, 1986), Chap. 6.
[68] K.-M. Chen, J. Chin. Chem. Soc. (Taipei) **49**, 723 (2002).
[69] E. Wigner and E. E. Witmer, Z. Phys. **51**, 859 (1928).
[70] D. H. Parker, Acc. Chem. Res. **33**, 563 (2000).
[71] A. T. J. B. Eppink, D. H. Parker, M. H. M. Janssen, B. Buijsse, and W. J. van der Zande, J. Chem. Phys. **108**, 1305 (1998).
[72] R. G. Bray and R. M. Hochstrasser, Mol. Phys. **4**, 1199 (1976).

Downloaded 02 Dec 2004 to 128.253.219.80. Redistribution subject to AIP license or copyright, see http://jcp.aip.org/jcp/copyright.jsp